INL/JOU-20-57316-Revision-0

In-situ construction of ceria-metal/titanate heterostructure with controllable architectures for efficient fuel electrochemical conversion

December 2021

Shuai He, Jianing Hui, Xiangling Yue, Meng Li

Changing the World's Energy Future

Idaho National Laboratory

INL/JOU-20-57316-Revision-0

In-situ construction of ceria-metal/titanate heterostructure with controllable architectures for efficient fuel electrochemical conversion

Shuai He, Jianing Hui, Xiangling Yue, Meng Li

December 2021

Idaho National Laboratory
Idaho Falls, Idaho 83415

http://www.inl.gov

Prepared for the
U.S. Department of Energy
Under DOE Idaho Operations Office
Contract DE-AC07-05ID14517

In-situ construction of ceria-metal/titanate heterostructure with controllable architectures for efficient fuel electrochemical conversion

Shuai He,[†] Meng Li,[‡] Jianing Hui,[†] and Xiangling Yue[, †]*

[†]School of Chemistry, University of St Andrews, St Andrews, Fife, KY16 9ST, UK

[‡]Energy and Environmental Science and Technology, Idaho National Laboratory, Idaho Falls, ID 83415, USA

*E-mail: xy57@st-andrews.ac.uk

ABSTRACT:

Construction of ceria-metal/titanate heterostructure *via* exsolution is a promising strategy to improve the catalytic activity of titanate perovskites and broaden their applications in various energy conversion scenarios. However, the species exsolved after reduction are limited to reducible metal cations, such as Ni, Co, Fe, and precious metals. Herein, we report a modified exsolution approach for co-exsolving active oxides and metal nanoparticles from a titanate perovskite, $La_{0.8}Ce_{0.1}Ni_{0.4}Ti_{0.6}O_{3-\delta}$ (LCeNT). We highlight strained facet-specific CeO_2 cubes can be grown on the support after an air-annealing process with their morphology tunable by varying annealing temperature, whilst exsolution of Ni nanoparticles form subsequently following chemical/electrical reduction. An electrolyte-supported SOFC utilizing CeO_2-Ni@LCeNT anode achieves maximum power density of 642 mW cm^{-2} at 900 ℃ in H_2 (~3% H_2O). Exceptional robustness of the heterostructure is illustrated after running the cell in CH_4 (~3% H_2O) for 20 h.

Overall, this work demonstrates an intriguing pathway to constructing stable and active ceria-metal/titanate heterostructure for energy applications.

KEYWORDS: titanate perovskite, CeO_2 exsolution, co-exsolution, tunable heterostructure, SOFCs

1. INTRODUCTION

Titanate perovskites consisting of various alkaline and/or rare earth metals at the A-site have been continuing to attract a great deal of attention in a variety of fields including catalysis and energy applications.[1-3] This is due to their capability of accommodating multiple oxidation states at the B-site, which catalyzes various oxidation/reduction reactions and provides superior conductivity.[4-7] Besides, titanates are relatively stable against carbon deposition and redox cycling, offering excellent efficiency and durability for long-term operation.[8-11] Nevertheless, the broad utilization of titanate is hindered by its insufficient electrocatalytic activity when compared with that of the conventional metal-based catalysts.[12, 13]

Modification of titanate to enhance its catalytic properties is therefore imperative to enable its wider application. Creating heterostructure is one of the predominant methods for fabricating highly active materials in catalytic and electrocatalytic systems. By carefully designing the heterointerface, the attributes of a heterostructure could be efficiently tuned. Impregnation is a widely used and economically feasible technique for dispersing nanoparticles (NPs) on titanate surface to build heterostructures. Titanates decorated with impregnated CeO_2-Ni nanostructures were reported to demonstrate substantially improved electrochemical performance for fuel oxidation, making them good candidates for electrochemical systems.[14-16] Lu et al. infiltrated CeO_2 and Ni NPs into a $La_{0.2}Sr_{0.25}Ca_{0.45}TiO_3$ (LSCT) backbone in an anode-

supported solid oxide fuel cell (SOFC), which exhibited a remarkably boosted electrochemical oxidation activity, achieving a peak power density of 0.96 W cm^{-2} at 800 °C in H_2.[16] Disturbingly, the infiltrated NPs are found prone to aggregating at elevated temperatures due to their weak particle-substrate interactions, leading to inevitable performance degradation with extended operation time. A heterostructure with thermodynamically stable catalyst NPs can be alternatively built by *in-situ* exsolution, which has attracted intensive interests in recent years due to the inherently stronger particle-substrate interaction and diverse catalyst components it introduced. So far, the studies have been focused on the exsolution of singular transitional metal or alloy catalysts from titanates.[17-21]

In this work, we aim to develop an approach to co-exsolve ceria and Ni nanoparticles and construct the ceria-Ni/titanate heterostructure *in situ* from a titanate substrate, $La_{0.8}Ce_{0.1}Ni_{0.4}Ti_{0.6}O_{3-\delta}$ (LCeNT). A previous report attempted to co-exsolve CeO_2-Ni NPs from the same titanate backbone by a single reduction treatment (1000 °C in 5% H_2/Ar),[17] however, despite a diffraction peak of ceria and that of metallic Ni detected by X-ray diffraction, CeO_2 nanostructure was never microscopically evidenced on the surface of the titanate and as such, application of this material with both ceria and Ni NPs from exsolution has not been reported to the best of the authors' knowledge. In contrast, the approach developed in the present work consists of an air-annealing process and a subsequent reduction treatment, from which nanoscale ceria cubes featuring $\{111\}_{CeO2}$ facets and Ni NPs were successfully constructed respectively on the surface of the parent titanate perovskite. The heterostructure, specifically the heterointerface between CeO_2 and LCeNT support, was tuned by varying annealing temperature, yielding different size and population in ceria nanocubes. The underlying mechanism for the controllable ceria exsolution was explored. The application of this new heterostructure was exemplified as a SOFC anode, with its performance and stability evaluated in H_2 and/or

CH_4 fuels. The contribution of the exsolved ceria nanostructure and the ceria-Ni/titanate heterostructure was assessed and discussed towards the electro-oxidation of H_2 and CH_4.

2. EXPERIMENTAL

2.1 Material synthesis and sample preparation

$La_{0.8}Ce_{0.1}Ni_{0.4}Ti_{0.6}O_3$ perovskite was fabricated *via* a modified solid-state synthesis method, following the procedures in Ref [11]. A stoichiometric amount of dried La_2O_3 (Pi-Kem, 99.99%), CeO_2 (Acros, 99.9%), $Ni(NO_3)_2 \cdot 6H_2O$ (Acros, 99%) and TiO_2 (Alfa Aesar, 99.6%) were mixed homogeneously, and after that, the mixture was calcined at 1000 ℃ for 12 hrs. The resultant precursor was ball-milled for 2 hrs, followed by a final firing at 1400 ℃ for 12 hrs to form a pure perovskite phase.

The as-synthesized LCeNT was ground in an agate mortar and then ball-milled with a planetary ball miller for 2 hrs to obtain fine powders with an average particle size of ~3 μm. The LCeNT fine powder was mixed with 10 wt.% rice starch (Sigma-Aldrich, US) as pore former and pressed into pellets, followed by calcination at 1400 ℃ for 2 hrs. The prepared pellets were annealed at different temperatures ranging from 800 ℃ to 1400 ℃ for 2 hrs in ambient air to study the effect of temperature on the segregation of ceria particles. The annealed samples were named with annealing temperature following LCeNT, *e.g.* LCeNT800, LCeNT1100, *etc*. thereafter. The generation of metallic Ni nanoparticles happened during a reduction of the annealed samples at 900 ℃ in 5% H_2/Ar flow. A sample without annealing treatment was also reduced under the same conditions, referred to as rLCeNT herein.

2.2 Material Characterizations

X-ray diffraction (XRD). Room temperature XRD was used to analyze the phase purity and crystal structure of the as-synthesized LCeNT powder and the LCeNT pellets annealed at

varying temperatures as well as after reduction. XRD measurement was done on a PANalytical Empyrean X-ray diffractometer with Cu-$K_{\alpha 1}$ radiation in reflection mode, and the samples were scanned from 10 to 90 degrees with a step size of 1.3 °/ min. The obtained XRD patterns were then analyzed with Xpert HighScore plus software to confirm the crystal structure. Selected data were refined using GSAS-II software to determine the unit cell parameters and the weight fraction of any secondary phase.[36] A set of refined parameters include linear background interpolation, scale factor, unit cell parameters, peak profile parameters *u*, *v,* and *w*, sample displacement, atomic positions, site occupancies, and thermal factor for individual atom sites.

Scanning electron microscopy (SEM). The surface morphology of the porous LCeNT pellets before and after annealing/reduction was characterized by a FEI Scios Dual-Beam Focused Ion Beam – Scanning Electron Microscope (FIB-SEM, FEI company, US). Backscattered electron (BSE) mode was adopted as well in some cases to highlight the compositional variation. The working voltage for imaging was 5 kV. Energy-dispersive X-ray analysis (EDS) was conducted at 15 kV to identify elemental compositions of a specific area. The studied pellets include as-prepared LCeNT (reference) and annealed LCeNT before and after reduction.

Scanning transmission electron microscopy (STEM). High resolution high-angle annular dark-field STEM (HAADF-STEM) imaging, EDS, and Electron energy loss spectra (EELS) analysis were performed at 200 kV using a scanning transmission electron microscope equipped with an objective Cs aberration corrector (FEI Titan Themis 200, fitted with a Super-X windowless EDX detector). TEM and EDS allow us to inspect the microstructural and compositional information of the material before and after various treatments, and EELS enables us to identify the valence state of Ce in the as-prepared and annealed LCeNT.

Thin LCeNT lamellae, as TEM/EDS/EELS sample, were prepared using the Scios microscope in FIB mode, at a voltage of 30 kV with Ga^+ ion source. A typical FIB milled lamella containing

desirable surface nanostructures is displayed in **Figure S1**. The final lamella was around 50 nm in thickness, ideal for further atomic resolution examination.

2.3 Electrochemical characterization

Fuel cell fabrication. $Zr_{0.89}Sc_{0.1}Ce_{0.01}O_{2-\gamma}$ (ScSZ) electrolyte (thickness in the range of 120 to 130 μm) was fabricated by tape casting and sintering at 1400 ℃. Electrodes having an active area of 0.5 cm^2 were introduced by screen-printing on both sides of the dense ScSZ electrolyte, which served as support to the electrodes. LCeNT ink was made by mixing the perovskite powder (average particle size ~3 μm) with dispersant and organic binder. $(La_{0.8}Sr_{0.2})_{0.95}MnO_3$ (LSM)-ScSZ (50:50 wt%) ink, as well as LSM ink, were prepared in a similar fashion. After screen printing, the LCeNT fuel electrode was fired at 1200 ℃ while the LSM based air electrode was fired at 1100 ℃. The thickness of both electrodes was in the range of 20-30 μm. Gold paste/wires were used for current collection on both fuel electrode and air electrode. An overview of the single cell can be found in **Figure S2**.

Electrochemical testing. The ScSZ-supported button cell was amounted to the testing jig and sealed with ceramic paste (Ceramabond 552, Aremco). The assembly was then placed in a vertical temperature-controlled furnace. Prior to the measurement, 5% H_2/N_2 (20 mL min^{-1}) was introduced to the anode side and maintained for 20 hrs at the operating temperature (900 ℃) to exsolve Ni nanoparticles. After this, humidified H_2 at a constant flow rate of 40 mL min^{-1} flowed to the anode for fuel cell performance evaluation. During the course of the electrochemical test, the air electrode was exposed to ambient air.

The chemical reduction of the perovskite to exsolve nanoparticles is a lengthy process (~20 hrs), and it has been found that applying a high electrolysis voltage, such as 2V during steam electrolysis operation, can almost instantly reduce the perovskite.[37, 38] Such an electrochemical

activation (EA) process was reported to produce sufficient B-site exsolution and thus reinforced fuel electrode performance. Therefore, sequential EA operations were employed to the LCeNT electrode at the operating temperature to boost the cell performance further. This was done in humidified H_2 (40 mL min^{-1}) at 2.0 V for a total of 20 min.

Impedance and current-voltage (I-V) characteristics of the cell were measured using a Solartron 1470B instrument coupled with a 1252A frequency response analyzer. Impedance data with AC voltage amplitude of 10 mV and frequency ranging from 100 kHz to 100 mHz were collected under open-circuit voltage conditions (OCV). After EA operation, IV and impedance measurements were performed to record the fuel cell's performance progression.

3. RESULTS AND DISCUSSION

3.1 Characteristics of pristine LCeNT

Figure 1a displays the Rietveld refined XRD characteristic reflections of the as-prepared LCeNT and rLCeNT at room temperature; a pure perovskite structure is seen for the pristine LCeNT, confirming the successful synthesis of the A-site deficient titanate in air. The pure phased titanate is further evidenced by its smooth and clean surface microstructure in **Figure 1b**, with compositions closely matching the expected stoichiometric ratio as measured using STEM-EDS (**Figure S3**). After reducing the as-prepared LCeNT in 5% H_2/Ar at 900 ℃ for 20 hrs, a small yet noticeable peak can be seen at 44.5^o in the XRD pattern in Figure 1a. It indicates the exsolution of Ni metal, which is accompanied by a slight lattice expansion (~0.42%) in perovskite. As a support to this, densely packed NPs can be seen on the surface of rLCeNT (in Figure 1c).

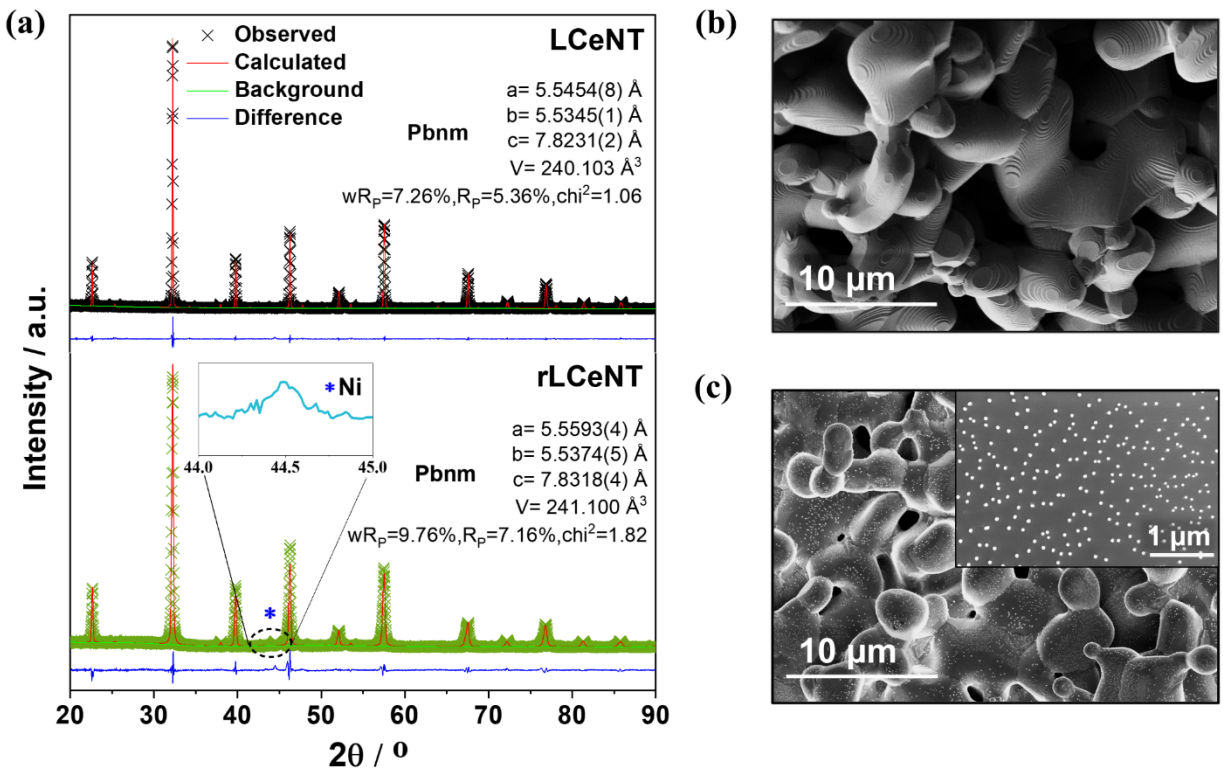

Figure 1. (a) Rietveld refined XRD patterns of the as-prepared LCeNT and rLCeNT; SEM micrographs of (b) the as-prepared LCeNT and (c) reduced LCeNT (rLCeNT) after flowing 5% H_2/Ar at 900 ℃ for 20 hrs

The absence of CeO_2 in both XRD and SEM-EDS (**Figure 1c** and **S4**) analysis of rLCeNT suggests no evident CeO_2 precipitation occurred after reduction under 5% H_2/Ar at 900 ℃ for 20 hrs. According to an early study, the co-exsolution of a fluorite-type structure (possibly CeO_2) and Ni was induced after reducing LCeNT at 1000 ℃ in a diluted hydrogen atmosphere.[15] It was assumed such fluorite phase reflected the possible presence of reduced $CeO_{2-\delta}$, which was triggered by the high local depletion of Ni on the B-site and the significant distortion in the perovskite caused by the undersized $Ce^{3+/4+}$. Nevertheless, no direct proof of microscopic observation of CeO_2 was provided in that study. This implies the exsolution of readily

observable CeO_2 phases is not guaranteed in reducing atmosphere at a lower temperature (*e.g.* 900 ℃ in our work). Alternatively, highly faceted CeO_2 cubes can be grown *in situ* by merely annealing the pristine LCeNT in the air, whilst a consecutive reduction treatment leads to the exsolution of metallic Ni nanoparticles on the perovskite surface. This will be discussed in detail in the following sections.

3.2 A-site exsolution of CeO_2 cubes

Annealing induced CeO_2 growth. Upon annealing the pristine LCeNT at 1200 ℃, numerous cube-like nanostructures (~220 nm in size) grow on the titanate surface in Figure 2a, which is a distinct feature comparing to the smooth surface microstructure of the as-prepared counterpart (Figure 1b). The distribution of the nanostructure appears to be uniform, preferentially anchored on the surface of the titanate grain rather than grain boundaries after annealing at 1200 ℃. As evidenced by the XRD analysis (in **Figure S5b**), the cube-like structure is most likely CeO_2 due to the appearance of its $\{111\}_{CeO2}$ reflection peak at 28.6°,[39] indicating the segregation of ceria from the perovskite lattice during annealing. It appears that the LCeNT perovskite structure only experiences a slight unit cell volume shrinkage (~0.11%) due to the segregation of CeO_2.

The faceted ceria cubes develop a well-socketed interface structure on the substrate without any visible cracks or voids, which is explicitly revealed by the cross-sectional STEM imaging in Figure 2b. The STEM-EDS analysis was performed at the CeO_2/LCeNT interface area to study the elemental distribution across the exsolved surface, and the results are illustrated in Figure 2(b, c). The EDS line scan spectrum and element maps prove that the cube consists of cerium and oxygen, with a ratio 1: 2 matching the stoichiometric value of ceria. It means that the Ce component in the exsolved cubes predominantly exists as Ce (IV).

High-resolution STEM imaging was conducted to investigate the crystalline structure of the exsolved CeO_2 cube, as shown in Figure 2(d, e). The atomic geometry of the faceted ceria cube is characterized by the densely packed and periodically arranged Ce atoms, and the fast Fourier transform (FFT) pattern of the ceria single-crystal implies its octahedral cubic structure. In addition, the edge lattice fringes of the ceria cube with the spacing of 0.348 nm and 0.305 nm can be indexed to $\{111\}_{CeO2}$ and $\{200\}_{CeO2}$ planes, respectively. Differing from randomly orientated ceria nanoparticles, the well-ordered ceria cubes consisting of multiple termination facets and orientations were suggested to possess two times higher activity per surface area for CO_2 conversion.[40] Comparing to a typical cubic cerium oxide, where $d_{\{111\}}$= 0.311 nm, $d_{\{200\}}$= 0.269 nm,[41] the lattice of the exsolved ceria cube seems to be notably expanded, indicating a strained crystal structure, which will be discussed further in the following part.

Figure 2 (f, g) presents the high-resolution STEM images of the interface between an exsolved CeO_2 cube and the LCeNT substrate. The measured lattice fringe spacings of 0.348 nm and 0.305 nm of the substrate can be indexed to the $\{111\}_{LCeNT}$ and the $\{200\}_{LCeNT}$ planes, respectively. These are identical to the values of the exsolved ceria single crystal, as shown in Figure 2 (d, e), indicating the epitaxial growth of CeO_2 cubes with an expanded lattice structure. The exsolution of ceria epitaxy, which is favorable thermodynamically, is to minimize the interfacial strain due to lattice mismatch between the two materials. As shown in Figure 2g, the atom geometry at a cube/substrate interfacial region exhibits an abrupt transition from one phase to the other with no observable micropores in between, suggesting a coherent interface structure. The close-packed Ce atoms well align to the B-site cations of the titanate, which reflects a parallel orientation relationship between the two lattices. A similar coherent heterointerface structure was observed by Neagu *et al.* at the epitaxially grown Ni/substrate interface.[31] Such well-pinned interface architecture was found to be beneficial not only for providing superior

stability of the exsolved nanoparticles against aggregation but also for facilitating ion interdiffusion process between the two phases.

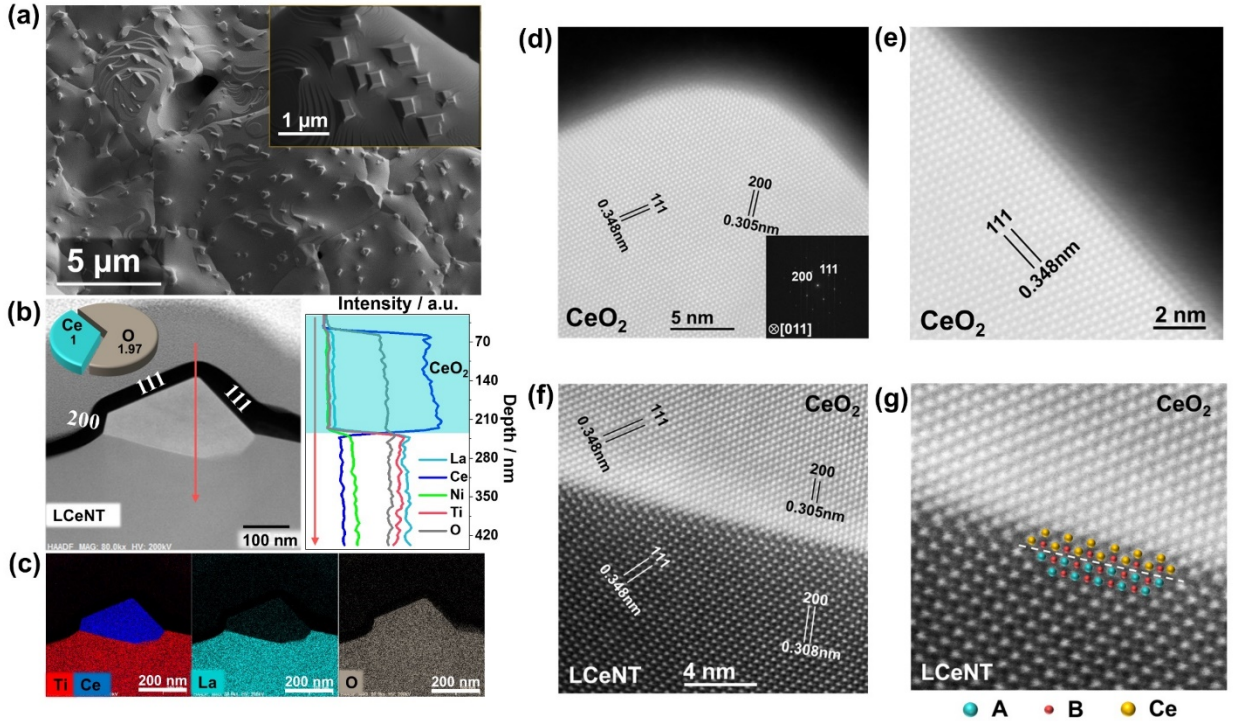

Figure 2. Microstructure and element distribution of LCeNT1200. (a) SEM micrographs of the titanate surfaces after annealing at 1200 ℃; (b) STEM-HAADF image of an exsolved ceria nanocube and the corresponding EDS line scan spectrum. The inserted arrows and pie chart indicate the direction of the corresponding EDS line scan, and the rough atomic ratio between Ce and O acquired through quantifying the EDS analysis, respectively; (c) STEM-EDS element mapping showing the element distribution across the exsolved titanate interface; (d, e) High-resolution STEM images of the terminating facets of an exsolved CeO_2 cube, taken along CeO_2[011] zone axis; (f, g) atomic geometry at the CeO_2/LCeNT interface.

Temperature-controlled ceria growth. The exsolution of ceria cubes from LCeNT is found sensitive to annealing temperatures, hence the microstructures of the as-synthesized LCeNT

annealed at different temperatures in the range of 1300-800 ℃ for a fixed 2 hrs duration were monitored. It is aimed that by adjusting the annealing conditions, ceria cubes with desirable size and surface coverage can be grown.

Figure 3 shows the BSE micrographs of the surface morphology of LCeNT annealed at 1300, 1200, 1100, 1000, 900, and 800 ℃ respectively, and **Figure 4 (a, b)** displays the corresponding XRD patterns after annealing at these temperatures. The behavior of ceria cube exsolution as a function of annealing temperature is illustrated by a schematic diagram shown on the right-hand side in Figure 3. Depending on the annealing conditions, the size of exsolved ceria cubes and their population vary greatly. At 1300 ℃, there are no obvious CeO_2 cubes emerging on the surface of the titanate grain. Nevertheless, some stripe-shaped ceria phase can be seen along the grain boundaries, which is confirmed by the appearance of a small peak at 28.5^o, corresponding to CeO_2, on the XRD pattern in Figure 4 a-b. **Figure 4c** illustrates the weight fraction of exsolved ceria and the corresponding unit cell shrinkage of the parent LCeNT as a function of annealing temperature, which is acquired based on the Rietveld refinement analysis of XRD patterns (**Figure S5**). Worth noting that the weight fraction of the ceria dopant in pristine LCeNT is approximately 7.6 wt.%. In comparison to the pristine LCeNT, there is around one-third of ceria segregated from the titanate (~2.7 wt.%) after annealing at 1300 ℃, with a ~0.16% cell volume shrinkage in perovskite accompanying ceria segregation. When annealing temperature drops to 1200 ℃, the exsolution of ceria can also be seen from the XRD pattern in Figure 4 (a-b). Still, the morphology of ceria displays pronounced faceting on the surface of the substrate grain in Figure 3. Comparing to 1300 ℃, lowering annealing temperature leads to a gradual decrease in the normalized intensity of the ceria diffraction peak in Figure 4b, indicating lowered ceria segregation extent with temperature, *e.g.*, ~1.4 wt.% of ceria weight fraction and 0.11% of perovskite volume shrinkage after annealing at 1200 ℃.

As the annealing temperature drops to 1100 ℃, substantial exsolution of fine CeO_2 cubes takes place on the titanate surface, as shown in the BSE image in Figure 3, revealing ceria cubes with a much smaller size (~130 nm *vs* ~220 nm) and larger population (~9 per μm^2 *vs* ~1 per μm^2) as compared to those after annealed at 1200 ℃. It should be noted that although the exsolution of ceria cubes at 1100 ℃ is seen under SEM, the diffraction peak of CeO_2 cannot be detected by XRD. This is most likely due to the low amount of ceria exsolved at low temperatures, which is lower than the detection limit of the diffractometer employed (<1 wt.%). Further decrease in annealing temperature gives rise to the formation of even smaller ceria cubes. However, the population does not tend to increase significantly (*e.g.* ~55 and ~40 nm in cube size, and ~20 and ~10 per μm^2 in cube density at 1000 and 900 ℃, respectively). The precipitation of CeO_2 cubes from the titanate perovskite seems to disappear after annealing at 800 ℃, which is possibly originated from the insufficient thermal energy for Ce^{4+} bulk diffusion and nucleation at such a low temperature.

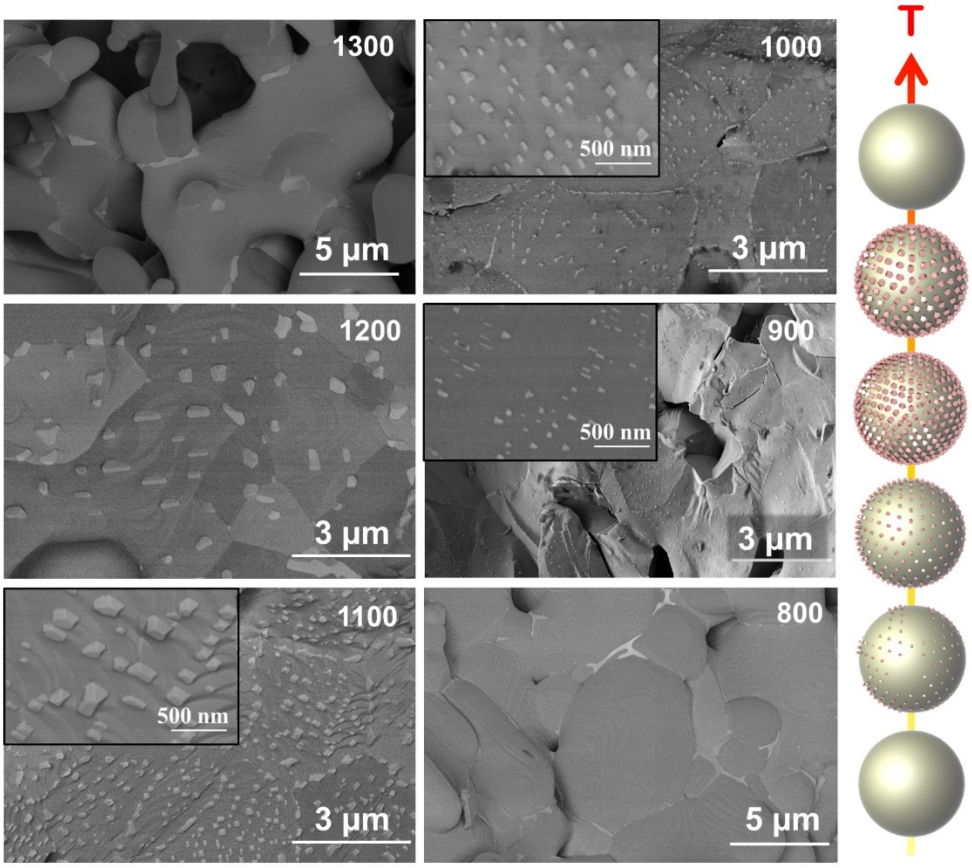

Figure 3. Backscattered electron micrographs of LCeNT surfaces annealed at 1300, 1200, 1100, 1000, 900, and 800 ℃ for 2 hrs in air respectively, and a schematic diagram showing the trend of CeO_2 cube growth as the temperature increases (from bottom to top).

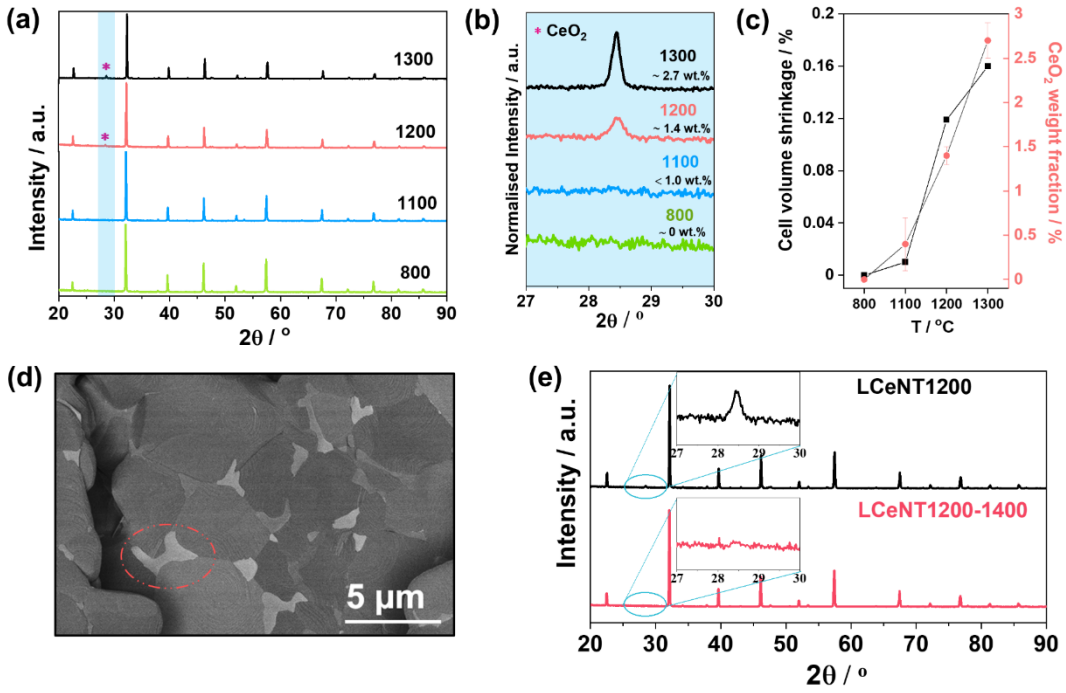

Figure 4. (a) XRD reflections of LCeNT annealed at 1300, 1200, 1100 and 800 ℃ for 2 hrs and (b) the magnified area showing CeO_2 (111) peak with rough quantification results obtained from Rietveld refinement, (c) LCeNT unit cell shrinkage following ceria exsolution as well as exsolved CeO_2 weight fraction as a function of annealing temperature, (d) BSE image of the LCeNT1200 surface after treated at 1400 ℃ for 2 hrs in air and (e) the corresponding XRD patterns. The dashed circle in (d) highlights the presence of a possible ceria phase.

To examine whether the exsolved CeO_2 phase is capable of being re-incorporated back into the underlying perovskite lattice, we fired the LCeNT1200 at 1400 ℃ in the air for 2 hrs, namely LCeNT1200-1400. Figure 4d shows the BSE image of the surface morphology of LCeNT1200-1400. After being subjected to high temperature again, the exsolved ceria cubes on the grain surfaces disappear, with some small patches of possible ceria phase (highlight by a dashed circle in Figure 4d) left at the grain boundaries of the substrate. Compared to

LCeNT1200, the absence of the ceria reflection peak in the XRD pattern in Figure 4e confirms that most of the exsolved ceria have re-incorporated into the underlying perovskite structure after being subjected to 1400 ℃.

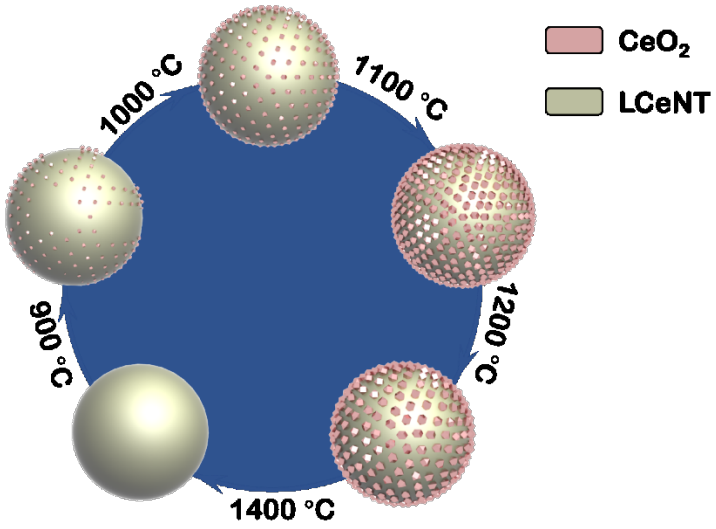

Figure 5. A schematic diagram of the proposed CeO_2-exsolution loop as a function of annealing temperature, demonstrating a viable pathway to constructing the surface nanostructure with desired particle coverage.

Herein, we propose a feasible method for adjusting the ceria exsolution by taking advantage of the annealing temperature, which could be used to grow CeO_2 cubes with desired size and population on the substrate surface. Since the exsolved ceria phase is re-dissolvable, it could be advantageous to regenerate the particle-substrate interfaces after degradation despite the high operation temperature required; however, this needs further investigation. A schematic diagram illustrating such a process is shown in **Figure 5**.

Mechanistic discussion of CeO_2 exsolution. Based on the results discussed so far, it appears that the incorporation of ceria in the titanate was successful at 1400 ℃ in the air during the initial synthesis, producing a pure orthorhombic perovskite structure. At lower temperatures (1300 ℃~ 900 ℃), up to one-third of doped ceria in LCeNT segregated from the perovskite lattice, which formed patch-like structure on the grain boundaries at 1300 ℃ and cubes on the grain surfaces of the substrate at lower than 1300 ℃. Upon firing at 1400 ℃ again, the segregated ceria can re-dissolve into the underlying titanate lattice. It seems temperature is a critical factor affecting the dissolution/segregation of ceria in titanate perovskite. Herein, we propose such an incorporation-segregation-dissolution cycle is a process involving (a) thermal reduction at high temperature during synthesis, (b) low-temperature oxidation, and (c) titanate lattice strain relaxation during annealing.

The incorporation of Ce in as-prepared LCeNT was naturally considered to be Ce (IV), as the titanate was fabricated in the air using CeO_2 as starting material.[15] However, Ce (IV) cations have been found too small to fit in the A-site of the titanate perovskite, which causes significant lattice strain and distortion.[42-44] Some researchers found in their study that ceria can only be successfully doped in titanate under a reducing atmosphere, with cerium preferentially occupying the A-site as Ce (III).[35, 44, 45] Indeed, the presence of Ce (III) in the pristine LCeNT is unambiguously revealed by the EELS analysis, as presented in **Figure 6a**, though cerium doping into A site in titanate was realized through the solid-state synthesis in the air in our work. The M_4, M_5 edges of Ce in EELS can provide information regarding its oxidation states, which has been utilized widely in many Ce-containing structures.[46, 47] In Figure 6a, the Ce M_4 edge is more asymmetrical than the M_5 edge, with a shoulder peak A at 896.4 eV; the branching ratio, *i.e.* peak intensity $I(M_5)/[I(M_4)+I(M_5)]$, of M_5: M_4 is close to 0.55. These features suggest the dominant presence of Ce (III) in pristine LCeNT. As a comparison, Figure 6b shows the EELS

spectrum of Ce acquired from an exsolved CeO_2 cube. The $M_{4,5}$ peaks of Ce in ceria cube can be identified by two shoulder peaks, B and B′, originated from transitions to 4f states in the conduction band;[48] the intensity of M_5 peak is lower than that of M_4, distinct from that of Ce (III). These characteristics denote the Ce (IV) nature of cerium in the exsolved nanostructures, consistent with the EDS analysis in Figure 2b.

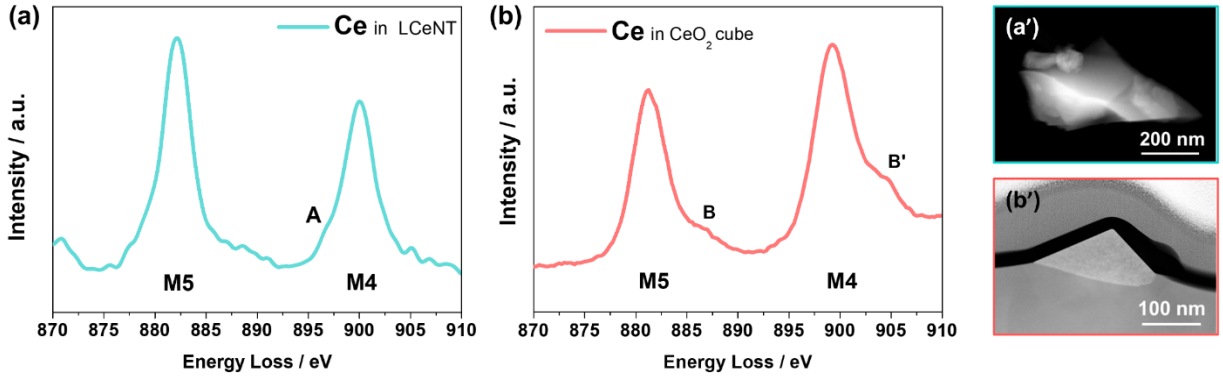

Figure 6. A comparison of Ce EELS spectra acquired from (a, a′) an as-prepared LCeNT particle and (b, b′) an exsolved ceria cube.

Cumming *et al.* [42, 49] also reported the presence of Ce^{3+} at A-site of the doped $SrTiO_3$ after sintering in the air at 1400 °C. It seems that Ce^{4+} is reduced to Ce^{3+} during synthesis to occupy the A-site of the titanate perovskite. Such a phenomenon, commonly referred to as thermal reduction, has been widely observed in many oxide systems, [50-55] which generally requires a high temperature (≥ 1400 °C) and a low oxygen partial pressure (<10^{-7} bar).[50] Gokon *et al.*[54] evaluated the activity of CeO_2 at thermal reduction temperatures of 1300-1500 °C for the two-step water-splitting reaction. The CeO_2 material treated at higher temperature was found to result in higher reduction extent and therefore, higher hydrogen production rate. Following several prerequisites, the thermal reduction process has been well explained by a charge compensation model proposed

by Peng et al.[56] In the case of La (III) substitution by Ce (IV) in the present work, the defect models describing the processes occurred during the synthesis of LCeNT can be written as:

(1)

(2)

(3)

During annealing LCeNT in the temperature range of 1300 ℃ to 900 ℃, the conditions required for thermal reduction no longer exist, on the contrary, oxidation of Ce^{3+} dopant in LCeNT occurs, generating many undersized Ce^{4+} cations on the A-site of the titanate (*i.e.* $r_{Ce4+,\ CN=12}$= 1.14 Å *vs* $r_{La3+,\ CN=12}$=1.36 Å). Such significant cation size discrepancy consequently drives the Ce^{4+} dopant out of the host lattice, with numerous patch and cube-like ceria precipitates exsolved on the titanate grain boundaries and surfaces, respectively, depending on temperature. When the annealing temperature decreases to below 900 ℃, the ambient environment cannot provide enough thermal energy for the above processes to proceed. Therefore, the ceria exsolution was not observed on the micrograph of LCeNT800 (Figure 3) nor the XRD pattern of LCeNT800 shown in Figure 4a-b.

Generally, the main driving forces for such cation segregation, *e.g.* Sr segregation,[59-66] are recognized as a combination of electrostatic interactions and elastic energy which results from cation size mismatch.[57, 58] Herein, to relax the elastic energy generated around the oxidized Ce dopants that are much smaller than the host ions, cation re-arrangement would occur spontaneously, leading to the segregation of CeO_2 on the surface. This process can be influenced by temperature, polarization, oxygen partial pressure, *etc.*,[59] thus could provide means for optimization to tune the material properties.

3.3 A-site CeO_2 and B-site Ni co-exsolution

Although ceria exsolution does not exert a significant impact on the LCeNT perovskite structure as revealed in Figure 4a, there could be a potential influence on the subsequent exsolution of Ni nanoparticles in reducing atmosphere. Therefore, SEM and STEM measurements were performed on the LCeNT1200 to examine its capability of releasing metallic Ni nanoparticles upon reduction.

Figure 7a displays the microstructure of the LCeNT1200 after reduction in 5% H_2/Ar at 900 ℃ for 20 hrs. It can be seen that a significant number of Ni nanoparticles (~50 nm, ~25 per μm^2) with an even distribution have formed on the surface of titanate perovskite. The inserted model in Figure 7a vividly illustrates the LCeNT backbone covered with uniformly exsolved CeO_2 and Ni nanoparticles. The exsolution of Ni nanoparticles was also observed on the LCeNT annealed at different temperatures (see **Figure S6)**. These indicate after the emergence of ceria cubes with varying extent, the annealed titanate is still able to form Ni nanoparticles on the surface of perovskite after reduction. STEM-EDS analysis was conducted at an exsolved interface to examine its element distribution with the results presented in **Figure 7(b, c).** The EDS element maps in Figure 7c confirm the presence of the faceted ceria cube and metallic Ni particles anchored on the titanate support. Worth mentioning that in addition to the surface exsolved Ni nanoparticles, there are a tremendous amount of Ni nanoparticles precipitated inside the perovskite. The bulk exsolved particles are much smaller than that of the surface counterparts (~20 nm *vs* ~50 nm, respectively). Although these particles are inaccessible to surface reactants, a recent report found that the endogenous exsolution of Ni nanoparticles remarkably enhanced the oxygen transport and exchange properties of the parent material for CH_4 conversion.[60]

Besides the formation of Ni nanoparticles, partial reduction of the CeO_2 cubes also occurs after the reduction treatment; from the EDS quantification analysis (Figure 7b), the atomic ratio

between Ce and O in the ceria cube rises to 1: 1.54. To examine the ceria/LCeNT interface stability against reducing atmosphere (5% H_2/Ar, 900 °C), we carried out high-resolution STEM inspection with the results shown in **Figure 7 d-f**. In Figure 7e, the lattice fringe alignment between CeO_{2-x} and the support is identical to that of the CeO_2/LCeNT interface before reduction. It seems the socketed particle-substrate interface structure is retained, despite the partial reduction of the ceria cube. Nevertheless, as highlighted by red arrows in Figure 7f, atomic distortions in the ceria lattice are observed. Such lattice defects are possibly due to the lattice strain accumulated during the reduction of the CeO_2 cube; the pinned CeO_2/LCeNT interface structure will likely be impaired in a more reducing environment.

On the other hand, the Ni/LCeNT interface is inspected by STEM imaging as well (in **Figure 7 g-i**). As displayed in **Figure 7g**, the exsolved Ni nanoparticle also develops sharp and pinned interface nanostructure with the parent perovskite. In the vicinity of the Ni/LCeNT interface region, the titanate lattice appears to have a brighter contrast comparing to its bulk lattice (shown in **Figure 7h**). This is possibly a result of the partial submergence of the Ni particle upon exsolution, which causes lattice superimposition. Worth mentioning that at the edge of the Ni/LCeNT interface in **Figure 7f**, a small 'neck' structure, which shares an identical atom arrangement to the host perovskite, tightly wraps up the Ni particle. The formation of the necking structure is likely due to the surface diffusion of the perovskite towards the Ni/LCeNT interface to minimize the surface energy of the system during Ni growth, similar to the particle sintering behavior reported in the literature.[61] These features of the exsolved interfaces are widely observed in many Ni exsolution-based systems and are believed to provide good anchorage for the metal particles to their host.[62, 63]

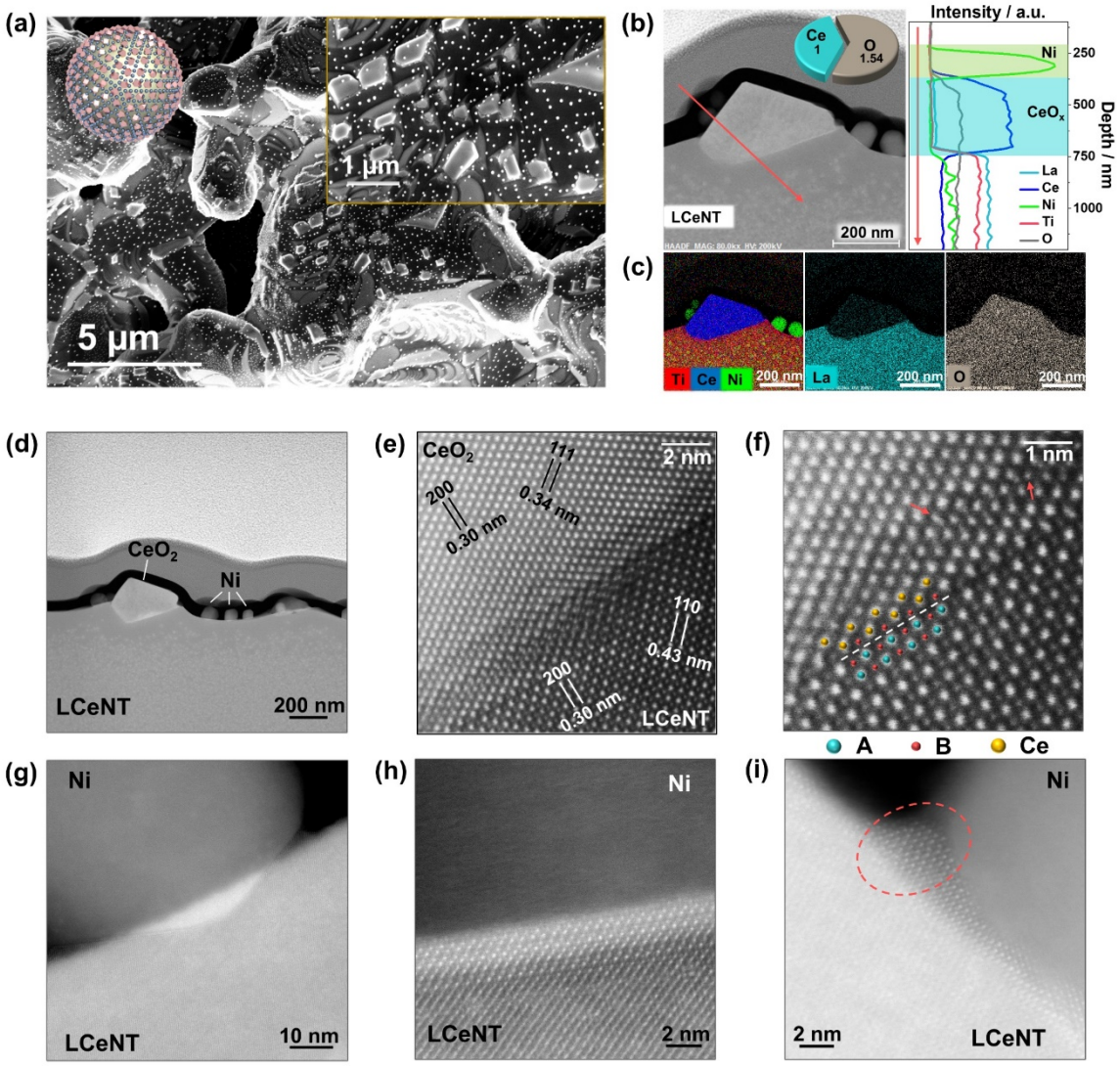

Figure 7. Microstructure and element distribution of LCeNT1200 after reduction at 900 ℃ for 20 hrs. (a) SEM micrographs of the titanate surfaces and the inserted model showing the exsolved titanate structure; (b) STEM-HAADF image of a CeO_{2-x} cube with exsolved Ni nanoparticles and the corresponding EDS line scan spectrum. The inserted arrows and pie chart indicate the direction of the corresponding EDS line scan, and the rough atomic ratio between Ce and O acquired through quantifying the EDS analysis, respectively; (c) STEM-EDS element mapping showing the element distribution across the exsolved titanate interface. High resolution STEM images at exsolved (d,e,f) CeO_2/LCeNT and (g,h,i) Ni/LCeNT interfaces. (e) Atomic

geometry at CeO_2/LCeNT interface and its magnified area shown in (f). The atomic arrangements of Ni/LCeNT interfaces are given in (h) central region and (i) edge region. The arrows in (f) point out two distinct atomic distortions near the interface, indicating strained ceria lattice. The dashed circle in (i) shows the neck formation at the interface edge due to perovskite surface diffusion.

3.4 Electrocatalytic performance of LCeNT as SOFC anode

Following the structural characterizations discussed earlier, the electro-oxidation activity of the LCeNT as anode material in SOFC applications was evaluated in H_2. It should be noted that CeO_2 cubes were introduced *in situ* on the LCeNT surface after the anode calcination stage (1200 ℃, see Experimental for details). The LCeNT anode, supported on the ScSZ electrolyte, was firstly reduced by 5% H_2/N_2 at 900 ℃ for 20 hrs to exsolve Ni nanoparticles. After the chemical reduction, the titanate electrode was further reduced electrochemically by applying a voltage of 2.0 V to the LCeNT cell in humidified H_2 for a total of 20 min. The electrochemical results, as well as the post-mortem microstructure of the LCeNT electrode, are presented in **Figure 8.**

Prior to the chemical reduction, the initial performance of the single cell is characterized by a considerable polarization resistance, R_P = 7.55 Ω cm^2 in 5% H_2/N_2, and an ohmic resistance ($R_Ω$) of 0.25 Ω cm^2 measured under OCV condition (**Figure 8a**). The $R_Ω$ is mainly originated from the 120 μm thick electrolyte at 900 ℃, as well as the lateral contribution from the LCeNT anode due to its low conductivity value (**Figure S7** and **Supplementary Note 1**). Upon reduction in 5% H_2/N_2, the R_P of the cell is substantially reduced to 3.13 Ω cm^2. This is due to the exsolution of abundant Ni nanoparticles on the anode surface, as evidenced in **Figure 8b**. In Figure 8b, the LCeNT electrode surface is uniformly decorated by a large number of Ni nanoparticles (~46

nm). The *in situ* growth of Ni nanocatalysts has been suggested to facilitate the hydrogen dissociation and diffusion processes, thus significantly enhancing the fuel cell's performance.[16, 64]

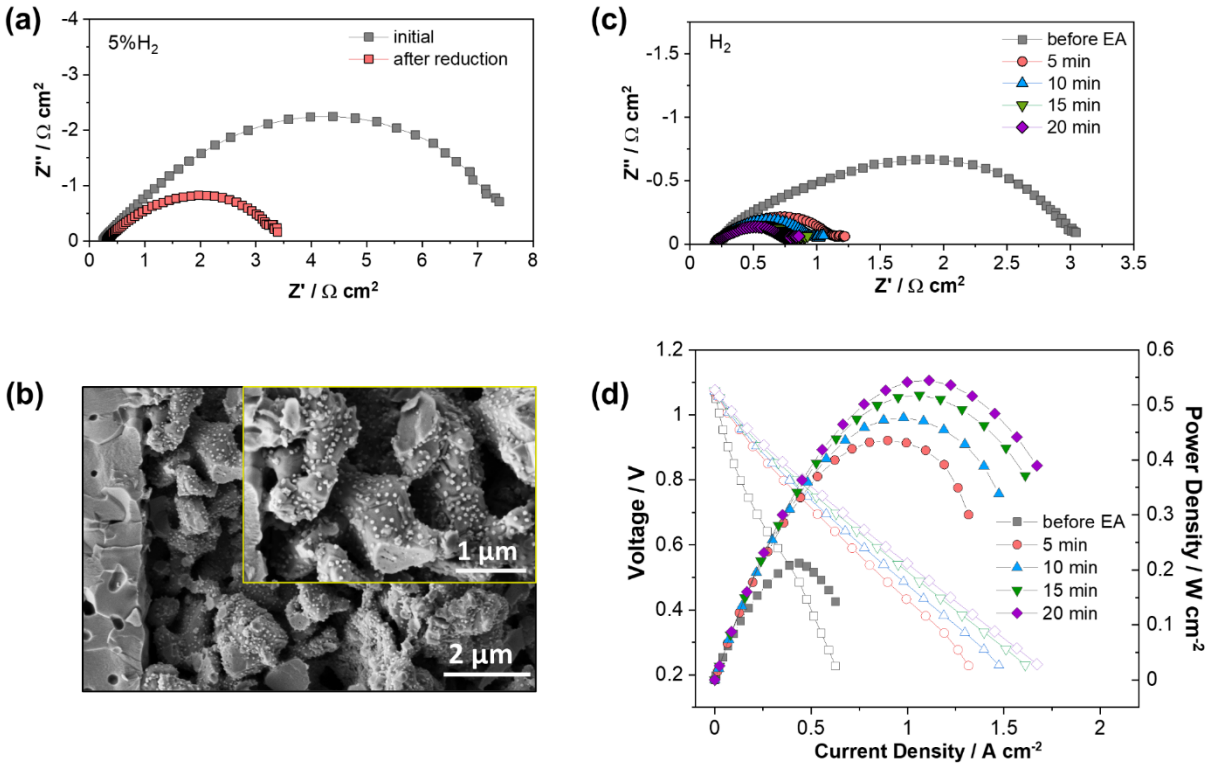

Figure 8. Electrolyte-supported LCeNT|ScSZ|LSM-ScSZ single cells. (a) Open circuit impedance spectrum of the single cell before and after reduction in 5% H_2/N_2 at 900 °C for 20 hrs and (b) SEM micrograph of the reduced LCeNT electrode; (c) open-circuit impedance spectrum and (d) I-V curves of the single cell during EA operation at 2.0 V in humidified H_2. All electrochemical measurements were performed at 900 °C.

After the chemical reduction, the LCeNT electrode is further activated by employing several short-term EA operations, *i.e.* applying 2 V to the cell. The EA treatment has been reported to reduce the perovskite electrode within several minutes, resulting in the exsolution of more yet

finer nanocatalysts and thus greatly improved electrode performance comparing to 20 hrs reduction in H_2 atmosphere.[37] Before the electrochemical reduction, the initial R_P of the LCeNT cell is measured to be 2.82 Ω cm^2 under OCV (Figure 8c). Upon EA for 5 min, a drastic reduction in R_P is seen, which drops rapidly by 65% to 0.98 Ω cm^2; the $R_Ω$ also decreases from 0.24 Ω cm^2 to 0.21 Ω cm^2. Following a couple of sequential EA treatments, the $R_Ω$ and R_P of the cell continue to decline slowly, with 0.20 Ω cm^2 and 0.59 Ω cm^2 obtained respectively at the end of the operation. As a result, the peak power density (PPD) of the cell surges to 545 mW cm^{-2}, increased by 153% of its initial value before the electrochemical reduction (215 mW cm^{-2} as shown in Figure 8d).

The chemically and electrochemically reduced LCeNT cell has so far demonstrated very competitive performance in humidified H_2 fuel, with the PPD outweighing many other similar single cells reported in the literature (see **Table S1**).[38, 65-70] To aid the comparison, the titanate electrodes reported in the literature are often modified by (1) impregnating or mixing with other catalysts such as CeO_2, Y_2O_3-ZrO_2 (YSZ) and/or Ni, *etc.*; [66, 68, 70, 71] (2) introducing a high dopant level on the B-site (*e.g.* 70% Fe *vs* 30% Ti, 0.37 W cm^{-2} at 900 °C);[67, 68] (3) pre-reduction at high temperatures (*e.g.* 1350 °C in 4% H_2/Ar, 0.51 W cm^{-2} at 900 °C);[65, 69] or (4) solely B-site exsolution of metal catalysts (*e.g.* Ni nanoparticles, 0.36 W cm^{-2} at 900 °C).[38] In other words, the co-exsolved LCeNT electrode, fabricated with ease and simplicity, substantiates itself as a promising anode candidate for effective electrochemical fuel oxidation in SOFCs.

4. CONCLUSIONS

In the present work, we demonstrated a viable approach to co-exsolving densely packed CeO_2 and Ni nanocatalysts *in situ* from a titanate perovskite backbone. We firstly highlighted that abundant growth of faceted CeO_2 cubes from the perovskite could be realized *via* a simple

annealing treatment (*e.g.* ~50 nm in size, ~20 per μm^2 in coverage at 1000 ℃), and a subsequent reduction treatment enabled the exsolution of densely packed Ni nanoparticles (~50 nm, ~25 per μm2 at 900 ℃) in 5% H_2/Ar.

We further revealed the close link between the ceria exsolution and the annealing temperature. The incorporation of ceria in the titanate was successful at 1400 ℃ in the air mainly due to a thermal reduction process. When annealed in the temperature range of 900 ℃ to 1300 ℃, up to one-third of doped ceria in LCeNT segregated from the perovskite lattice, which formed cubes on the grain surfaces of the support at lower than 1300 ℃ and patch-like structure on the grain boundaries at 1300 ℃. Upon firing at 1400 ℃ again, the exsolved ceria re-dissolved into the underlying titanate lattice. Hence, by making use of the annealing temperature, we proposed a facile method for adjusting the ceria growth with varying coverage and sizes. The underlying mechanism for such a ceria exsolution behavior was proposed due to the low-temperature oxidation of Ce (III) and subsequent titanate lattice strain relaxation.

Finally, the exsolved LCeNT was evaluated as a potential fuel electrode in ScSZ electrolyte-supported SOFC applications. The chemically and electrochemically reduced LCeNT electrode yielded a satisfactory maximum power density of 545 mW cm^{-2} at 900 ℃ in 3% H_2O/H_2, a competitive value that surpasses many infiltrated counterparts reported in the literature. It thus demonstrated the promising application of the exsolved LCeNT as, but not limited to fuel electrode material in SOFCs.

In a word, we believe that the surface re-structuring strategy exemplified here, *i.e.* CeO_2-Ni co-exsolution, sets a facile example to construct nanoscale-active architecture and provides insights for the future design of more sophisticated oxide systems.

ASSOCIATED CONTENT

Supporting Information Available: evidence of the reversibility of ceria exsolution, XRD patterns of the single-phase LCeNT variants, XRD patterns of ceria (111) characteristic peaks obtained from LCeNT annealed at varying temperature, atomistic geometry of the ceria cube, and its interface with the host. (PDF)

AUTHOR INFORMATION

Corresponding Author

Xiangling Yue – *School of Chemistry, University of St Andrews, St Andrews, United Kingdom, KY16 9ST*; E-mail: xy57@st-andrews.ac.uk

Author Contributions

The manuscript was written through the contributions of all authors. All authors have given approval to the final version of the manuscript.

Notes

The authors declare no competing financial interest.

ACKNOWLEDGMENTS

The authors would like to thank the EPSRC UKRI Innovation Fellowship EP/S001891/1 for funding, and the EPSRC Capital for Great Technologies Grant EP/L017008/1 for financial support.

REFERENCES

(1) Kanhere, P.; Chen, Z. A Review on Visible Light Active Perovskite-Based Photocatalysts. *Molecules* **2014,** *19*, 19995-20022.
(2) Stramare, S.; Thangadurai, V.; Weppner, W. Lithium Lanthanum Titanates: A Review. *Chem. Mater.* **2003,** *15*, 3974-3990.
(3) Yoo, K. B.; Choi, G. M. Performance of La-Doped Strontium Titanate (Lst) Anode on Lagao3-Based Sofc. *Solid State Ionics* **2009,** *180*, 867-871.
(4) Sunarso, J.; Hashim, S. S.; Zhu, N.; Zhou, W. Perovskite Oxides Applications in High Temperature Oxygen Separation, Solid Oxide Fuel Cell and Membrane Reactor: A Review. *Prog. Energy Combust. Sci.* **2017,** *61*, 57-77.
(5) Deak, D. S. Strontium Titanate Surfaces. *Mater. Sci. Technol.* **2013,** *23*, 127-136.
(6) Alvarado Flores, J. J.; Ávalos Rodríguez, M. L.; Andrade Espinosa, G.; Alcaraz Vera, J. V. Advances in the Development of Titanates for Anodes in Sofc. *Int. J. Hydrogen Energy* **2019,** *44*, 12529-12542.
(7) Jiang, S. P.; Chan, S. H. A Review of Anode Materials Development in Solid Oxide Fuel Cells. *J. Mater. Sci.* **2004,** *39*, 4405-4439.
(8) Hui, S.; Petric, A. Electrical Properties of Yttrium-Doped Strontium Titanate under Reducing Conditions. *J. Electrochem. Soc.* **2002,** *149*, J1-J10.
(9) Atkinson, A.; Barnett, S.; Gorte, R. J.; Irvine, J. T.; McEvoy, A. J.; Mogensen, M.; Singhal, S. C.; Vohs, J. Advanced Anodes for High-Temperature Fuel Cells. *Nat. Mater.* **2004,** *3*, 17-27.
(10) Rothschild, A.; Menesklou, W.; Tuller, H. L.; Ivers-Tiffée, E. Electronic Structure, Defect Chemistry, and Transport Properties of Srti1-Xfexo3-Ysolid Solutions. *Chem. Mater.* **2006,** *18*, 3651-3659.
(11) Neagu, D.; Irvine, J. T. S. Structure and Properties of La0.4sr0.4tio3ceramics for Use as Anode Materials in Solid Oxide Fuel Cells. *Chem. Mater.* **2010,** *22*, 5042-5053.
(12) Marina, O. Thermal, Electrical, and Electrocatalytical Properties of Lanthanum-Doped Strontium Titanate. *Solid State Ionics* **2002,** *149*, 21-28.
(13) Neagu, D.; Irvine, J. T. S. Enhancing Electronic Conductivity in Strontium Titanates through Correlated a and B-Site Doping. *Chem. Mater.* **2011,** *23*, 1607-1617.
(14) Irvine, J. T. S.; Neagu, D.; Verbraeken, M. C.; Chatzichristodoulou, C.; Graves, C.; Mogensen, M. B. Evolution of the Electrochemical Interface in High-Temperature Fuel Cells and Electrolysers. *Nat. Energy* **2016,** *1*, 15014.
(15) Neagu, D.; Tsekouras, G.; Miller, D. N.; Menard, H.; Irvine, J. T. In Situ Growth of Nanoparticles through Control of Non-Stoichiometry. *Nat. Chem.* **2013,** *5*, 916-23.
(16) Sun, Y.; Li, J.; Zeng, Y.; Amirkhiz, B. S.; Wang, M.; Behnamian, Y.; Luo, J. A-Site Deficient Perovskite: The Parent for in Situ Exsolution of Highly Active, Regenerable Nano-Particles as Sofc Anodes. *J. Mater. Chem. A* **2015,** *3*, 11048-11056.
(17) Kwon, O.; Sengodan, S.; Kim, K.; Kim, G.; Jeong, H. Y.; Shin, J.; Ju, Y. W.; Han, J. W.; Kim, G. Exsolution Trends and Co-Segregation Aspects of Self-Grown Catalyst Nanoparticles in Perovskites. *Nat. Commun.* **2017,** *8*, 15967.
(18) Tsekouras, G.; Neagu, D.; Irvine, J. T. S. Step-Change in High Temperature Steam Electrolysis Performance of Perovskite Oxide Cathodes with Exsolution of B-Site Dopants. *Energy Environ. Sci.* **2013,** *6*, 256-266.
(19) Zhu, T.; Troiani, H. E.; Mogni, L. V.; Han, M.; Barnett, S. A. Ni-Substituted Sr(Ti,Fe)O3 Sofc Anodes: Achieving High Performance Via Metal Alloy Nanoparticle Exsolution. *Joule* **2018,** *2*, 478-496.
(20) Abanades, S.; Flamant, G. Thermochemical Hydrogen Production from a Two-Step Solar-Driven Water-Splitting Cycle Based on Cerium Oxides. *Sol. Energy* **2006,** *80*, 1611-1623.
(21) Montini, T.; Melchionna, M.; Monai, M.; Fornasiero, P. Fundamentals and Catalytic Applications of Ceo2-Based Materials. *Chem. Rev.* **2016,** *116*, 5987-6041.

(22) Kašpar, J.; Fornasiero, P.; Hickey, N. Automotive Catalytic Converters: Current Status and Some Perspectives. *Catal. Today* **2003,** *77*, 419-449.
(23) Faur Ghenciu, A. Review of Fuel Processing Catalysts for Hydrogen Production in Pem Fuel Cell Systems. *Curr. Opin. Solid State Mater. Sci.* **2002,** *6*, 389-399.
(24) Ramírez-Cabrera, E.; Atkinson, A.; Chadwick, D. Catalytic Steam Reforming of Methane over Ce0.9gd0.1o2−X. *Appl. Catal., B* **2004,** *47*, 127-131.
(25) Chan, S. H. S.; Yeong Wu, T.; Juan, J. C.; Teh, C. Y. Recent Developments of Metal Oxide Semiconductors as Photocatalysts in Advanced Oxidation Processes (Aops) for Treatment of Dye Waste-Water. *J. Chem. Technol. & Biot.* **2011,** *86*, 1130-1158.
(26) Murray, E. P.; Tsai, T.; Barnett, S. A. A Direct-Methane Fuel Cell with a Ceria-Based Anode. *Nature* **1999,** *400*, 649-651.
(27) Burnat, D.; Nurk, G.; Holzer, L.; Kopecki, M.; Heel, A. Lanthanum Doped Strontium Titanate - Ceria Anodes: Deconvolution of Impedance Spectra and Relationship with Composition and Microstructure. *J. Power Sources* **2018,** *385*, 62-75.
(28) Liu, Z.; Ding, D.; Liu, B.; Guo, W.; Wang, W.; Xia, C. Effect of Impregnation Phases on the Performance of Ni-Based Anodes for Low Temperature Solid Oxide Fuel Cells. *J. Power Sources* **2011,** *196*, 8561-8567.
(29) Kurokawa, H.; Sholklapper, T. Z.; Jacobson, C. P.; De Jonghe, L. C.; Visco, S. J. Ceria Nanocoating for Sulfur Tolerant Ni-Based Anodes of Solid Oxide Fuel Cells. *Electrochem. Solid-State Lett.* **2007,** *10*.
(30) Lu, L.; Ni, C.; Cassidy, M.; Irvine, J. T. S. Demonstration of High Performance in a Perovskite Oxide Supported Solid Oxide Fuel Cell Based on La and Ca Co-Doped Srtio3. *J. Mater. Chem. A* **2016,** *4*, 11708-11718.
(31) Neagu, D.; Oh, T. S.; Miller, D. N.; Menard, H.; Bukhari, S. M.; Gamble, S. R.; Gorte, R. J.; Vohs, J. M.; Irvine, J. T. Nano-Socketed Nickel Particles with Enhanced Coking Resistance Grown in Situ by Redox Exsolution. *Nat. Commun.* **2015,** *6*, 8120.
(32) Ye, L.; Zhang, M.; Huang, P.; Guo, G.; Hong, M.; Li, C.; Irvine, J. T.; Xie, K. Enhancing Co2 Electrolysis through Synergistic Control of Non-Stoichiometry and Doping to Tune Cathode Surface Structures. *Nat. Commun.* **2017,** *8*, 14785.
(33) Papaioannou, E. I.; Neagu, D.; Ramli, W. K. W.; Irvine, J. T. S.; Metcalfe, I. S. Sulfur-Tolerant, Exsolved Fe–Ni Alloy Nanoparticles for Co Oxidation. *Top. Catal.* **2018,** *62*, 1149-1156.
(34) Marina, O. A.; Pederson, L. R. In *Novel Ceramic Anodes for Sofcs Tolerant to Oxygen, Carbon and Sulfur*, The Fifth European Solid Oxide Fuel Cell Forum, 2002; J Huijismans. European Fuel Cell Forum. Switzerland: Lucerne: 2002; pp 481-489.
(35) Périllat-Merceroz, C.; Gauthier, G.; Roussel, P.; Huvé, M.; Gélin, P.; Vannier, R.-N. Synthesis and Study of a Ce-Doped La/Sr Titanate for Solid Oxide Fuel Cell Anode Operating Directly on Methane. *Chem. Mater.* **2011,** *23*, 1539-1550.
(36) Toby, B. H.; Von Dreele, R. B. Gsas-Ii: The Genesis of a Modern Open-Source All Purpose Crystallography Software Package. *J. Appl. Crystallogr.* **2013,** *46*, 544-549.
(37) Myung, J. H.; Neagu, D.; Miller, D. N.; Irvine, J. T. Switching on Electrocatalytic Activity in Solid Oxide Cells. *Nature* **2016,** *537*, 528-531.
(38) Chanthanumataporn, M.; Hui, J.; Yue, X.; Kakinuma, K.; Irvine, J. T. S.; Hanamura, K. Electrical Reduction of Perovskite Electrodes for Accelerating Exsolution of Nanoparticles. *Electrochim. Acta* **2019,** *306*, 159-166.
(39) WoŁcyrz, M.; Kepinski, L. Rietveld Refinement of the Structure of Ceoci Formed in Pd/Ceo2 Catalyst: Notes on the Existence of a Stabilized Tetragonal Phase of La2o3 in Lapdo System. *J. Solid State Chem.* **1992,** *99*, 409-413.
(40) Kovacevic, M.; Mojet, B. L.; van Ommen, J. G.; Lefferts, L. Effects of Morphology of Cerium Oxide Catalysts for Reverse Water Gas Shift Reaction. *Catal. Lett.* **2016,** *146*, 770-777.
(41) Akita, T.; Okumura, M.; Tanaka, K.; Kohyama, M.; Haruta, M. Tem Observation of Gold Nanoparticles Deposited on Cerium Oxide. *J. Mater. Sci.* **2005,** *40*, 3101-3106.
(42) Cumming, D. J.; Kharton, V. V.; Yaremchenko, A. A.; Kovalevsky, A. V.; Kilner, J. A. Electrical Properties and Dimensional Stability of Ce-Doped Srtio3−Δ for Solid Oxide Fuel Cell Applications. *J. Am. Ceram. Soc.* **2011,** *94*, 2993-3000.

(43) Subodh, G.; James, J.; Sebastian, M. T.; Paniago, R.; Dias, A.; Moreira, R. L. Structure and Microwave Dielectric Properties of Sr2+Nce2ti5+No15+3n(N≤ 10) Homologous Series. *Chem. Mater.* **2007,** *19*, 4077-4082.
(44) Zhou, X.-W.; Sun, Y.-F.; Wang, G.-Y.; Gao, T.; Chuang, K. T.; Luo, J.-L.; Chen, M.; Birss, V. I. Synthesis and Electrocatalytic Performance of La0.3ce0.1sr0.5ba0.1tio3 Anode Catalyst for Solid Oxide Fuel Cells. *Electrochem. Commun.* **2014,** *43*, 79-82.
(45) Sun, Y.-F.; Zhou, X.-W.; Zeng, Y.; Amirkhiz, B. S.; Wang, M.-N.; Zhang, L.-Z.; Hua, B.; Li, J.; Li, J.-H.; Luo, J.-L. An Ingenious Ni/Ce Co-Doped Titanate Based Perovskite as a Coking-Tolerant Anode Material for Direct Hydrocarbon Solid Oxide Fuel Cells. *J. Mater. Chem. A* **2015,** *3*, 22830-22838.
(46) Xu, H.; Wang, Y. Electron Energy-Loss Spectroscopy (Eels) Study of Oxidation States of Ce and U in Pyrochlore and Uraninite – Natural Analogues for Pu- and U-Bearing Waste Forms. *J. Nucl. Mater.* **1999,** *265*, 117-123.
(47) Garvie, L. A. J.; Buseck, P. R. Determination of Ce4+/Ce3+ in Electron-Beam-Damaged Ceo2 by Electron Energy-Loss Spectroscopy. *J. Phys. Chem. Solids* **1999,** *60*, 1943-1947.
(48) Karnatak, R. C.; Esteva, J.; Dexpert, H.; Gasgnier, M.; Caro, P. E.; Albert, L. X-Ray Absorption Studies of Ceo2, Pro2, and Tbo2. I. Manifestation of Localized and Extended F States in the 3d Absorption Spectra. *Phys Rev B Condens Matter* **1987,** *36*, 1745-1749.
(49) Cumming, D. J. Cerium-Doped Strontium Titanate Materials for Solid Oxide Fuel Cells. **2009**.
(50) Kodama, T.; Gokon, N. Thermochemical Cycles for High-Temperature Solar Hydrogen Production. *Chem. Rev.* **2007,** *107*, 4048-77.
(51) Sturzenegger, M.; Nüesch, P. Efficiency Analysis for a Manganese-Oxide-Based Thermochemical Cycle. *Energy* **1999,** *24*, 959-970.
(52) Lundberg, M. Model Calculations on Some Feasible Two-Step Water Splitting Processes. *Int. J. Hydrogen Energy* **1993,** *18*, 369-376.
(53) Lorentzou, S.; Karagiannakis, G.; Dimitrakis, D.; Pagkoura, C.; Zygogianni, A.; Konstandopoulos, A. G. Thermochemical Redox Cycles over Ce-Based Oxides. *Energy Procedia* **2015,** *69*, 1800-1809.
(54) Gokon, N.; Sagawa, S.; Kodama, T. Comparative Study of Activity of Cerium Oxide at Thermal Reduction Temperatures of 1300–1550 °C for Solar Thermochemical Two-Step Water-Splitting Cycle. *Int. J. Hydrogen Energy* **2013,** *38*, 14402-14414.
(55) Bulfin, B.; Lowe, A. J.; Keogh, K. A.; Murphy, B. E.; Lübben, O.; Krasnikov, S. A.; Shvets, I. V. Analytical Model of Ceo2 Oxidation and Reduction. *J. Phys. Chem. C* **2013,** *117*, 24129-24137.
(56) Peng, M.; Pei, Z.; Hong, G.; Su, Q. Study on the Reduction of Eu3+→Eu2+ in Sr4al14o25: Eu Prepared in Air Atmosphere. *Chem. Phys. Lett.* **2003,** *371*, 1-6.
(57) Lee, W.; Han, J. W.; Chen, Y.; Cai, Z.; Yildiz, B. Cation Size Mismatch and Charge Interactions Drive Dopant Segregation at the Surfaces of Manganite Perovskites. *J. Am. Chem. Soc.* **2013,** *135*, 7909-25.
(58) Koo, B.; Kim, K.; Kim, J. K.; Kwon, H.; Han, J. W.; Jung, W. Sr Segregation in Perovskite Oxides: Why It Happens and How It Exists. *Joule* **2018,** *2*, 1476-1499.
(59) Friedel, J. Electronic Structure of Primary Solid Solutions in Metals. *Adv. Phys.* **1954,** *3*, 446-507.
(60) Kousi, K.; Neagu, D.; Bekris, L.; Papaioannou, E.; Metcalfe, I. S. Endogenous Nanoparticles Strain Perovskite Host Lattice Providing Oxygen Capacity and Driving Oxygen Exchange and Ch4 Conversion to Syngas. *Angew Chem Int Ed Engl* **2019**.
(61) Cologna, M.; Raj, R. Surface Diffusion-Controlled Neck Growth Kinetics in Early Stage Sintering of Zirconia, with and without Applied Dc Electrical Field. *J. Am. Ceram. Soc.* **2011,** *94*, 391-395.
(62) Neagu, D.; Kyriakou, V.; Roiban, I. L.; Aouine, M.; Tang, C.; Caravaca, A.; Kousi, K.; Schreur-Piet, I.; Metcalfe, I. S.; Vernoux, P.; van de Sanden, M. C. M.; Tsampas, M. N. In Situ Observation of Nanoparticle Exsolution from Perovskite Oxides: From Atomic Scale Mechanistic Insight to Nanostructure Tailoring. *ACS Nano* **2019,** *13*, 12996-13005.
(63) He, S.; Chen, K.; Saunders, M.; Li, J.; Cui, C. Q.; Jiang, S. P. A Fib-Stem Study of La0.8sr0.2mno3 Cathode and Y2o3-Zro2/Gd2o3-Ceo2 Electrolyte Interfaces of Solid Oxide Fuel Cells. *J. Electrochem. Soc.* **2017,** *164*, F1437-F1447.

(64) Gao, Y.; Chen, D.; Saccoccio, M.; Lu, Z.; Ciucci, F. From Material Design to Mechanism Study: Nanoscale Ni Exsolution on a Highly Active a-Site Deficient Anode Material for Solid Oxide Fuel Cells. *Nano Energy* **2016,** *27*, 499-508.
(65) Ma, Q.; Iwanschitz, B.; Dashjav, E.; Mai, A.; Tietz, F.; Buchkremer, H.-P. Electrochemical Performance and Stability of Electrolyte-Supported Solid Oxide Fuel Cells Based on Y-Substituted Srtio3 Ceramic Anodes. *Solid State Ionics* **2014,** *262*, 465-468.
(66) Verbraeken, M. C.; Iwanschitz, B.; Mai, A.; Irvine, J. T. S. Evaluation of Ca Doped La0.2sr0.7tio3as an Alternative Material for Use in Sofc Anodes. *J. Electrochem. Soc.* **2012,** *159*, F757-F762.
(67) Cao, Z.; Zhang, Y.; Miao, J.; Wang, Z.; Lü, Z.; Sui, Y.; Huang, X.; Jiang, W. Titanium-Substituted Lanthanum Strontium Ferrite as a Novel Electrode Material for Symmetrical Solid Oxide Fuel Cell. *Int. J. Hydrogen Energy* **2015,** *40*, 16572-16577.
(68) Cho, S.; Fowler, D. E.; Miller, E. C.; Cronin, J. S.; Poeppelmeier, K. R.; Barnett, S. A. Fe-Substituted Srtio3−Δ–Ce0.9gd0.1o2 Composite Anodes for Solid Oxide Fuel Cells. *Energy Environ. Sci.* **2013,** *6*.
(69) Park, B. H.; Choi, G. M. Electrochemical Performance and Stability of La0.2sr0.8ti0.9ni0.1o3-Δ and La0.2sr0.8ti0.9ni0.1o3-Δ - Gd0.2ce0.8o2-Δ Anode with Anode Interlayer in H2 and Ch4. *Electrochim. Acta* **2015,** *182*, 39-46.
(70) Sun, X.; Wang, S.; Wang, Z.; Ye, X.; Wen, T.; Huang, F. Anode Performance of Lst–Xceo2 for Solid Oxide Fuel Cells. *J. Power Sources* **2008,** *183*, 114-117.
(71) Xu, J.; Zhou, X.; Dong, X.; Pan, L.; Sun, K. Catalytic Activity of Infiltrated La0.3sr0.7ti0.3fe0.7o3−–Ceo2 as a Composite Sofc Anode Material for H2 and Co Oxidation. *Int. J. Hydrogen Energy* **2017,** *42*, 15632-15640.